PHYSICAL SCIENCES

Large-scale synthesis of crystalline g-C_3N_4 nanosheets and high-temperature H_2 sieving from assembled films

Luis Francisco Villalobos[1], Mohammad Tohidi Vahdat[1,2], Mostapha Dakhchoune[1], Zahra Nadizadeh[1], Mounir Mensi[3], Emad Oveisi[4], Davide Campi[2], Nicola Marzari[2], Kumar Varoon Agrawal[1]*

Poly(triazine imide) (PTI), a crystalline g-C_3N_4, hosting two-dimensional nanoporous structure with an electron density gap of 0.34 nm, is highly promising for high-temperature hydrogen sieving because of its high chemical and thermal robustness. Currently, layered PTI is synthesized in potentially unsafe vacuum ampules in milligram quantities. Here, we demonstrate a scalable and safe ambient pressure synthesis route leading to several grams of layered PTI platelets in a single batch with 70% yield with respect to the precursor. Solvent exfoliation under anhydrous conditions led to single-layer PTI nanosheets evidenced by the observation of triangular g-C_3N_4 nanopores. Gas permeation studies confirm that PTI nanopores can sieve He and H_2 from larger molecules. Last, high-temperature H_2 sieving from PTI nanosheet–based membranes, prepared by the scalable filter coating technique, is demonstrated with H_2 permeance reaching 1500 gas permeation units, with H_2/CO_2, H_2/N_2, and H_2/CH_4 selectivities reaching 10, 50, and 60, respectively, at 250°C.

INTRODUCTION

Crystalline, nanoporous two-dimensional nanosheets, defined as nanometer-thick sheets hosting an array of precisely defined molecular-sized pores, offer highly accessible functional surface with a large surface area and are ideal for hosting and manipulating molecules (*1*–*4*). Attributing to their nanoporous structure, they can separate a molecular mixture by size sieving, a property that can be exploited in gas and liquid separation (*5*–*9*), selective ion transport (*10*), core-shell catalysis (*11*), and sensors (*12*). One of the most appealing promises of these nanosheets is that one can potentially fabricate membrane by a facile assembly of nanosheets (*13*–*15*), making them advantageous to the conventional molecular sieving membranes, which often involve a complex synthesis process. Crystalline g-C_3N_4, and in particular poly(triazine imide) (PTI) (*16*, *17*), is extremely appealing for this because it is composed of atom-thick layers, where each layer is atomically flat and hosts a high density of triangular gas-sieving nanopores with an effective pore aperture of 0.34 nm. Attributing to their crystalline carbon nitride framework, PTI can withstand harsh chemical conditions (*18*) as well as temperatures up to 600°C (*19*), making it appealing for sieving applications under harsh conditions. For instance, high-temperature H_2 purification from streams containing CO_2, N_2, and CH_4 using high-performance membranes, yielding a high H_2 permeance (transmembrane pressure–normalized flux) and selectivity, is expected to improve the energy efficiency of the industrial processes that generate and consume H_2. Examples include H_2/CO_2 and H_2/N_2 separation from the product of steam reforming of hydrocarbons, purging CH_4 and Ar from the recycle stream in ammonia synthesis and recovery of H_2 from the industrial off-gas (*20*–*23*). The state-of-the-art membranes for hydrogen sieving at high temperature are based on rigid polymers such as polybenzimidazole (PBI) (*24*, *25*), zeolites (*14*, *26*, *27*), amorphous silica (*28*–*30*), and dense Pd films (*31*–*33*). PBI membranes yield low H_2 permeance, while the Pd-based membranes suffer from stability issue in the presence of contaminants (H_2S, CO, and hydrocarbons). The silica and zeolite-based membranes show attractive performance for H_2 sieving; however, they involve a complex synthesis and activation process (*34*). In this context, the prospect of developing hydrogen-selective two-dimensional nanosheets that can enable membrane fabrication by the facile assembly techniques is highly attractive.

To the best of our knowledge, the single-layer PTI nanosheet, characterized by its unique triangular nanoporous structure, formed by imide-bridged triazine units, have not been reported. Advances in exfoliation of PTI have led to the synthesis of few-layered nanosheets. Electron microscopy of PTI nanosheets in these reports revealed a honeycomb structure, characteristic of PTI bilayer or multilayers due to the AB stacking of PTI layers (*19*, *35*, *36*). On the other hand, several reports claiming the synthesis and exfoliation of g-C_3N_4 actually dealt with polymeric melon, which is not fully condensed within the layer with heptazine units in each layer held together by weak intralayer hydrogen bonds (Supplementary Note I) (*37*).

A major challenge in the wide-scale adoption of PTI nanosheets is that the layered PTI (precursor to nanosheets) is synthesized in a complicated vacuum ampule–based solid-state synthesis route with a milligram yield (*16*, *36*). The scale-up of vacuum ampule–based synthesis is extremely difficult and can be potentially unsafe. Here, we demonstrate a facile synthesis route for highly crystalline layered PTI platelets using an ambient pressure synthesis condition yielding several grams of platelets in a single batch with 70% yield with respect to the precursor. A simple exfoliation route, based on stirring in anhydrous dimethylacetamide (DMAc), is reported, which leads to a high percentage of single-layer nanosheets, confirmed by the observation of the triangular pores of PTI by electron microscopy. Last, thin membranes are prepared, which could separate H_2 from CO_2, N_2, and CH_4, reaching a high hydrogen permeance of 1500 gas permeation units (GPUs; 1 GPU = 3.35×10^{-10} mol m^{-2} s^{-1} Pa^{-1}) at 250°C.

[1]Laboratory of Advanced Separations (LAS), École Polytechnique Fédérale de Lausanne (EPFL), Sion, Switzerland. [2]Theory and Simulation of Materials (THEOS) and National Centre for Computational Design and Discovery of Novel Materials (MARVEL), EPFL, Lausanne, Switzerland. [3]Institute of Chemical Sciences and Engineering (ISIC), EPFL, Sion, Switzerland. [4]Interdisciplinary Centre for Electron Microscopy (CIME), EPFL, Lausanne, Switzerland.
*Corresponding author. Email: kumar.agrawal@epfl.ch

RESULTS

Atom-thick nanoporous PTI nanosheets

Single-layer PTI nanosheets contain a high density of triangular nanopores that can accommodate a spherical guest with diameter below 0.34 nm (Fig. 1, A and B). Our ab initio calculations show that He and H_2 (kinetic diameters of 0.26 and 0.29 nm, respectively) can freely pass through the nanopore, while CH_4 (kinetic diameter of 0.38 nm) can only pass through single-layer PTI in a certain orientation (Supplementary Note II). To realize the corresponding sieving effect, it is crucial to synthesize highly crystalline PTI nanosheets without structural disorder, requiring advances in the crystallization of layered PTI and subsequent exfoliation to single layers. These advances are also expected to benefit other applications, e.g., energy storage and conversion (*36*, *38*), gas sensors (*39*, *40*), etc. (*37*).

Scalable ambient pressure synthesis of PTI platelets

The conventional synthesis of PTI is done by heating a mixture of the precursor (i.e., melamine, dicyandiamide, cyanamide, or urea) and a eutectic mixture of LiCl and KCl salts in a quartz ampule under a closed vacuum system. During the synthesis, the eutectic salt mixture melts, increasing the mobility of the g-C_3N_4 intermediates. The increased mobility is generally believed to be critical for ordering of the intermediates and their subsequent condensation (*16*). The sealed ampule is reported to be important because it prevents the escape of the intermediates (*18*, *41*, *42*). However, the ampule-based synthesis is complicated, can be unsafe because of the buildup of ammonia (can reach up to 12 bar), typically yields only 60 to 80 mg of crystalline PTI/Li^+Cl^-, and is a bottleneck for the scale-up of PTI. The synthesis of crystalline PTI using scalable ambient pressure conditions has remained elusive, producing amorphous PTI instead when the quartz ampule (vacuum) is substituted with a ceramic crucible (ambient pressure) (*18*).

By engineering the reaction conditions, mainly by confining the PTI precursor below the layer of salt, we could synthesize several grams of crystalline PTI at ambient pressure in a single batch foregoing the need of a quartz ampule (Fig. 1C). Briefly, a precursor (melamine) was placed at the bottom of a crucible, which was then covered completely with the salts. The crucible was heated to 600°C at ambient pressure, and PTI was collected by washing the salt by water. The resulting material [70% yield with respect to (w.r.t.) melamine] exhibited crystallinity similar to PTI synthesized using an ampule containing well-mixed reactants under vacuum (Fig. 1D, fig. S1, and table S1). The interlayer spacing indicated by the (002) peak was 3.36 Å, similar to graphitic materials. Overall, confining precursor below the salt bed was sufficient to maintain the needed concentration of partially condensed yet volatile intermediate precursors (e.g., melam) for the synthesis of crystalline PTI. We observed that the salt layer remained separated from the precursor/PTI layer (Fig. 1C). The fact that it was possible to obtain high-quality PTI crystals without mixing the precursor with the salts negates the hypothesis that the molten salts are the necessary solvent for the transport of intermediates (*16*, *17*). Therefore, the role of salts must be to guide the condensation of melam in an ordered structure. The ambient pressure synthesis in an open system allows one to synthesize PTI in less specialized laboratories and is expected to help the scalable production of PTI.

The as-synthesized material was a plate-shaped, hexagonal prismatic crystal with an average lateral size of 33 nm (SD = 21 nm; fig. S2). The lateral size of the layered platelets could be increased to 95 nm (SD = 60 nm) by using the as-synthesized platelets as seeds (Fig. 1E).

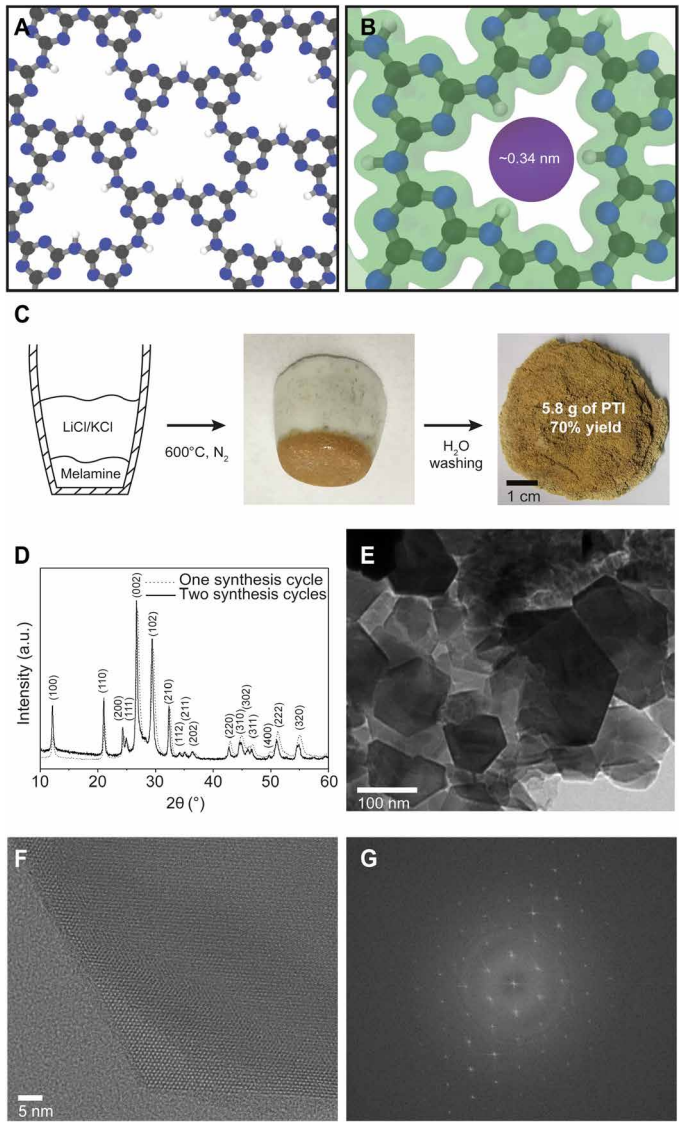

Fig. 1. Scalable synthesis of PTI layers. (**A**) Structure of the PTI layer. C, N, and H atoms are colored in gray, blue, and white, respectively. (**B**) Electron density isosurface of a PTI nanopore revealing the electron density gap in PTI nanopore. (**C**) Schematic of the synthesis of crystalline PTI under the ambient pressure condition with pictures showing the high yield of layered PTI (brownish in color). Photo credit: Luis Francisco Villalobos, École Polytechnique Fédérale de Lausanne. (**D**) Powder XRD pattern of the layered PTI. a.u., arbitrary units. (**E**) TEM images of PTI crystallites obtained after two synthesis cycles. (**F**) HRTEM image of the edge of a PTI crystal, revealing a honeycomb structure as a result of the AB stacking of layers. (**G**) Corresponding fast Fourier transform. An HRTEM image of the center of the same PTI crystal is available in fig. S5.

Repeating the growth cycles proved to be much more effective compared to increasing the growth time for increasing the platelet size (figs. S3 and S4). High-resolution transmission electron microscopy (HRTEM) image of a platelet revealed the uniform honeycomb-like pore channel in the layered sheets, which exists because of the AB stacking of the sheets (Fig. 1F). Consistent with x-ray diffraction (XRD) data, the platelets were highly crystalline (Fig. 1G), and lattice fringes were visible throughout the platelets (fig. S5). We did not detect any amorphous domains.

Exfoliation of PTI platelets

PTI crystals were exfoliated by stirring them in anhydrous DMAc at 100°C (fig. S6). It was possible to observe exfoliated nanosheets even after 6 hours. With 2 days of stirring, the suspension changed from yellow to cream (Fig. 2A). The resulting suspension consisted of a large population of the exfoliated nanosheets, which were then purified by centrifugation (Fig. 2B). The exfoliation produced a solution with a concentration of 0.14 ± 0.06 mg/ml. The selected-area electron diffraction (SAED) pattern of the PTI nanosheets was consistent with the expected hexagonal symmetry of a PTI layer (inset of Fig. 2B). An atomic force microscopy (AFM) study revealed a mean height of 0.77 nm, with most of the nanosheets being single layer (Fig. 2, C and D). In general, the single-layer nanosheets were smaller in the lateral size. HRTEM images confirmed the presence of single-layer PTI, where the characteristic triangular porous structure of PTI was observed (Fig. 2, E and F, and fig. S7). The few-layer nanosheets showed the expected honeycomb pattern formed by the AB stacking of the layers (Fig. 2, G and H, and fig. S8). X-ray photoelectron spectroscopy (XPS) measurements on a film made with these nanosheets revealed reduced Li^+ and Cl^- concentrations of 2.8 and 0.2 atomic %, respectively, compared to 5 atomic % (for both) in the layered PTI platelets (fig. S9, A and B, and table S2). The concentration of single-layer sheets could be further improved by centrifugation-based purification. In this case, Li^+ was not detected by XPS (fig. S9, C and D). This is expected because Li^+ and Cl^- reside in the nanopore and the gallery, respectively, and are more accessible for exchange upon exfoliation (*36*, *43*).

The nanosheet dispersion was stable for several months, indicating a similar surface energy between DMAc and PTI (*44*). We postulate that the interaction between Li^+ located in the PTI layers and DMAc played an important role in exfoliation. The carbonyl oxygen of DMAc interacts strongly with Li^+ and can form very stable complexes (*45*), potentially weakening the interlayer interaction. Exfoliation was not observed when anhydrous DMAc was not used. A similar but less pronounced effect has been observed for the dissolution of cellulose, where the DMAc-Li complex plays a crucial role and can be affected by the incorporation of water molecules into the solvation shell of lithium ions (*46*). Aprotic organic solvents, including DMAc, *N*-methylpyrrolidone, *N*,*N*-dimethylformamide, and dimethyl sulfoxide (DMSO), have been used in the past to exfoliate g-C_3N_4 including PTI; however, room temperature conditions led to stacks of two or more nanosheets (modal number 8 or 9 nanosheets) (*19*). Recently, using metallic sodium forming sodium naphthalide, Jia *et al.* (*35*) charged the PTI framework, and using DMAc as the solvent, they obtained nanosheets with an average thickness of 1.1 nm, although triangular pores expected from single-layer PTI were not detected in HRTEM. Overall, the method presented here is facile, leading to primarily single layers with an average thickness of 0.77 nm.

Potential of PTI nanosheets for molecular separations

Density functional theory (DFT) calculations of the interaction of He, H_2, N_2, and CH_4 with single-layer PTI sheets indicate that the triangular-shaped nanopores of PTI are attractive for the purification of H_2 from N_2 and CH_4 (Fig. 3A and fig. S10). H_2 and He can freely diffuse across the nanopore, attributing to their small size. N_2, when it orients itself such that the two nitrogen atoms are positioned perpendicular to the pore, does not experience a repulsion

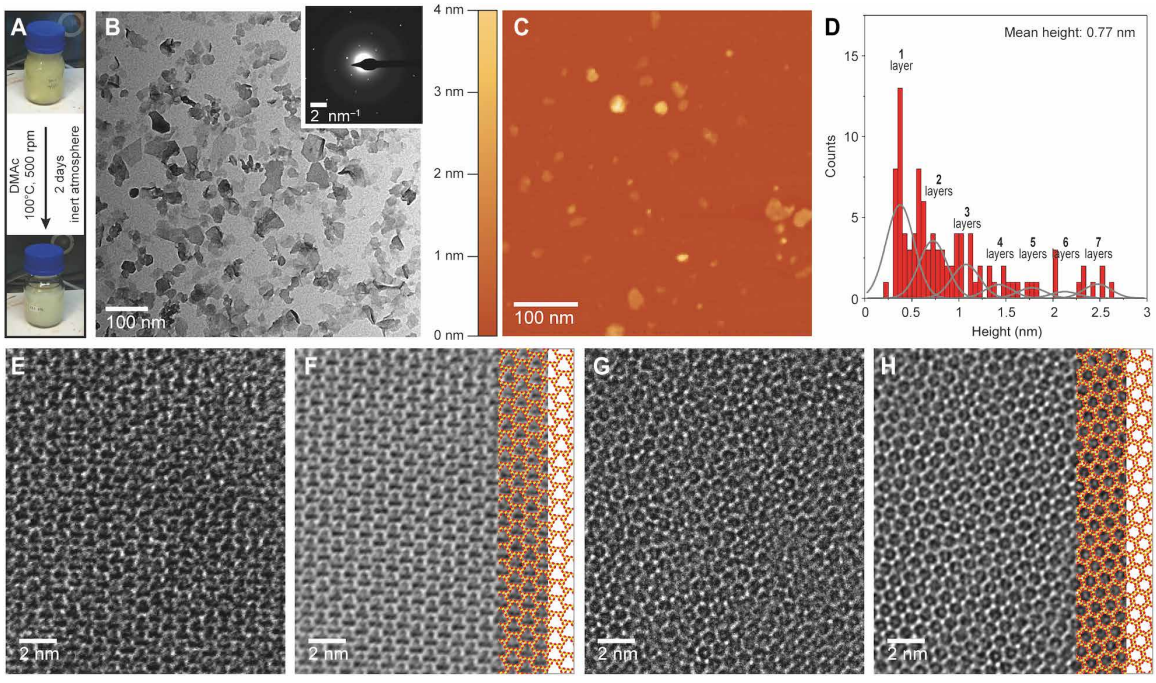

Fig. 2. Mild exfoliation of PTI. (**A**) Diagram showing the color of the PTI dispersion before and after exfoliation. Photo credit: Luis Francisco Villalobos, École Polytechnique Fédérale de Lausanne. (**B**) Bright-field TEM image of the dispersion of PTI nanosheets after 2 days of exfoliation inside an anhydrous DMAc solution at 100°C and a centrifugation-based purification. Inset shows a SAED pattern of a PTI nanosheet. (**C**) AFM image of PTI nanosheets. (**D**) Nanosheet thickness histogram ($n > 100$). A sum of Gaussians with a full width at half maximum of 0.35 nm shows the approximate range of bins that correspond to each number of layers. (**E**) HRTEM image of a single-layer PTI nanosheet and (**F**) its corresponding filtered image with the structure of single-layer PTI superimposed (C and N atoms colored in red and yellow, respectively). (**G**) HRTEM image of a few-layered PTI nanosheet and (**H**) its corresponding filtered image with the structure of bilayer PTI superimposed (C and N atoms colored in red and yellow, respectively).

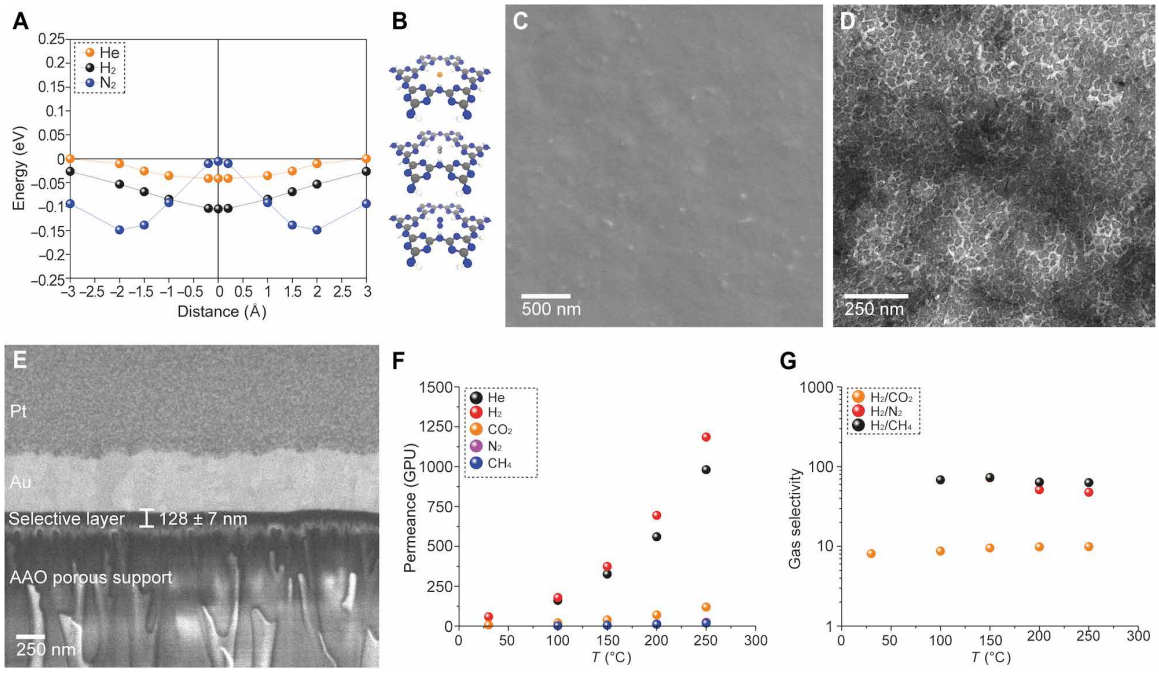

Fig. 3. Molecular sieving from PTI. (**A**) PES for He, H_2, and N_2 on a PTI monolayer. (**B**) Orientation of He, H_2, and N_2 at the center of the PTI nanopore. (**C**) SEM image of the PTI nanosheet film incorporating *m*-PBI chains as spacers. (**D**) Bright-field TEM image of the freestanding PTI/*m*-PBI film. (**E**) Cross section of the membrane revealing a 128-nm-thick selective layer. AAO, anodic aluminum oxide. (**F**) Permeance of He, H_2, CO_2, N_2, and CH_4 as a function of temperature and (**G**) corresponding H_2/CH_4, H_2/N_2, and H_2/CO_2 ideal selectivities.

at the center of the pore (Fig. 3B). However, the interaction energy of N_2 at the pore center is much lower than that at the absorbed state above the pore. As a result, it requires an activation energy of 0.145 eV to diffuse the nanopores. Therefore, PTI nanopores are expected to be hydrogen selective.

To understand the sieving capability of the PTI nanopores, we compacted the exfoliated PTI nanosheets in a 900-nm-thick film by vacuum filtration on a commercial Anopore support (fig. S11). The films were composed of well-packed, *c*-out-of-plane oriented, and overlapping crystalline PTI nanosheets. The transport of gas molecules with kinetic diameter up to 0.33 nm (He, 0.26 nm; H_2, 0.29 nm; CO_2, 0.33 nm) was in the temperature-activated regime (fig. S12A), with the activation energy increasing with the molecular size (activation energies of 20, 23, and 39 kJ mol^{-1} for He, H_2, and CO_2, respectively; fig. S12B and Supplementary Note III). The permeance of larger molecules (N_2, CH_4, and SF_6 with kinetic diameters of 0.36, 0.38, and 0.55 nm, respectively) did not increase with temperature, confirming that their transport took place solely through the packing defects. A tortuous gas transport through intersheet gallery spacing is not expected, as a *d* spacing of 0.32 to 0.34 nm was observed in the packed films (fig. S11F), corresponding to an impermeable gap of ca. 0.10 nm between the layers. As a result, H_2/N_2 and H_2/CH_4 selectivities (7.5 and 11.7, respectively) were considerably greater than the corresponding Knudsen selectivities (3.7 and 2.8, respectively).

The activated transport of hydrogen observed from the stacked nanosheet film is in contrast to the DFT calculations on single-layer PTI, indicating that in the stacked films, the molecules experienced an additional resistance to diffuse. This can be attributed to partial or complete blocking of a number of transport channels in the PTI film as a result of nonaligned nanosheet stacking or from residual Li^+ ion in the vicinity of some nanopores (Supplementary Note IV). Nonetheless, the transport study from stacked PTI nanosheets confirmed that the PTI nanosheets can sieve H_2 from N_2 and CH_4.

PTI membranes using PBI chains as spacers

To overcome the nanopore blockage by nonaligned stacking of nanosheets to some extent, we used *meta*-PBI (*m*-PBI) chains as spacers between the PTI nanosheets (Supplementary Note V). This was implemented by adding *m*-PBI to the dispersion of PTI nanosheets with a PTI/*m*-PBI ratio of 16:84 in the coating suspension. Because vacuum filtration was used for the film fabrication, the concentration of PTI in the assembled film is expected to be much higher than 16% because most of the *m*-PBI chains should be filtered out. Scanning electron microscopy image of films prepared in this manner indicated a uniform PTI coating on the support (Fig. 3C). TEM image of the film, transferred from the support to a TEM grid, confirmed a high packing density of PTI nanosheets (Fig. 3D). Owing to the filtration-based coating, the nanosheets appeared to orient *c*-out-of-plane perpendicular to the gas transport pathway across the film. The thickness of the film was 128 ± 7 nm (Fig. 3E).

Overall, the H_2 separation performance of PTI films improved when the *m*-PBI chains were incorporated in the film (Fig. 3, F and G, and fig. S12). The permeance of N_2 and CH_4 at 30°C was below the detection limit of the mass spectroscope. The membrane could be operated at 250°C, the limit of our membrane sealant. Attractive H_2 permeance (900 to 1450 GPUs; table S3) and corresponding H_2/CO_2, H_2/N_2, and H_2/CH_4 selectivities of 10, 48, and 63, respectively, were realized. High selectivities were observed at all temperatures (Fig. 3G). These membranes could find applications in regulating the H/N ratio in ammonia synthesis and in hydrogen purification after the water-gas shift reaction (*21*). We note that the hydrogen permeability of these ultrathin membranes at 250°C, ca. 180 Barrer, is much higher than

that reported for *m*-PBI membranes, establishing that the transport was dominated by PTI. For example, Dye and co-workers (*25*) reported H_2 permeability of ca. 12 Barrer at 250°C from a 4-μm-thick PBI membrane. Li *et al.* (*47*) reported H_2 permeability of ca. 77 Barrer at 250°C from a 22-μm-thick *m*-PBI film.

To evaluate the performance of PBI-impregnated PTI membranes in a more realistic mixture conditions, we tested the membrane using a 50:50 mixture feed of H_2 and N_2 at 250°C (fig. S13). The H_2 permeance and the H_2/N_2 separation factors were consistent with that of the single-gas test. The membranes could be pressurized to 5 bar (close to the limit of our setup; fig. S13A), where the H_2/N_2 selectivity was maintained at ca. 50 at all pressures.

The membranes prepared in this work were made on Anopore supports because they fulfill the following requirements: (i) they are stable in DMAc; (ii) they are stable at high temperatures; (iii) they host a small pore size, making it easier to retain small PTI nanosheets; and (iv) they have a smooth surface. We envision that the polymer-based solvent resistant nanofiltration membranes or scalable ceramic supports, which match the above criteria, will be a great alternative to Anopore to produce PTI membranes at a practical scale.

DISCUSSION

Overall, we report a large-scale synthesis strategy for PTI layers and single-layer PTI nanosheets, which are desired for catalysis and molecular sieving applications. We demonstrate that the PTI nanosheet–based membranes are attractive for high-temperature hydrogen sieving, while they provide a significant processability advantage compared to the conventional high-performance hydrogen-sieving membranes.

MATERIALS AND METHODS

Synthesis of PTI

Inside an Ar-filled glove box, 22.65 g of LiCl (Sigma-Aldrich) and 27.35 g of KCl (Sigma-Aldrich) were mixed and grinded to make the eutectic salt mix used for the synthesis. A 15-ml porcelain crucible (Morgan Advanced Materials) was filled with 0.5 g of melamine (Sigma-Aldrich) in the bottom and then covered completely with 12 g of the salt mix without mixing. The crucible was covered with its porcelain cap and transferred to a quartz tube furnace with an inner diameter (ID) of 120 mm (MTI Corporation, Richmond, CA). The sample was heated to 600°C (10°C/min) under N_2 flow (2 liters/min) and maintained at 600°C for a certain amount of time (fig. S3) and then cooled down to room temperature (10°C/min). It was washed with hot water at least three times to remove the salt mix completely and then dried at 120°C under vacuum. The second synthesis cycle to increase the size of PTI crystals was done in the same way, but instead of putting just melamine at the bottom, a mixture of 0.1 g of PTI powder from the first cycle and 0.5 g of melamine was grinded together and used. The protocol reported by Wirnhier *et al.* (*16*) was used for the synthesis of PTI inside a vacuum-sealed quartz ampule.

Scale-up of PTI

The same protocol used for preparing small batches (0.5 g of melamine, 15-ml crucible) was used to prepare larger batches using a 250-ml crucible (Fisher Scientific) and 8.3 g of melamine. The melamine-to-salt ratio was kept the same as for the small batches. The same heating and purification protocols were also used. The resulting material was as crystalline as when the synthesis was done in small batches, proving the scalability of the proposed ambient pressure synthesis approach for crystalline PTI. The yield was the same as for the small batches (i.e., 70% w.r.t. melamine).

Exfoliation of PTI

Inside an Ar-filled glove box, 100 mg of PTI was put inside a glass vial containing 100 ml of anhydrous DMAc (Fluorochem). The solution was heated to 100°C and stirred at 500 rpm for 2 days. The color of the solution changed from yellow to cream during this time. Last, the resulting solution was purified by three centrifugation steps of 10 min each at 5000*g*, 10,000*g*, and 15,000*g*, respectively, to obtain in the supernatant predominantly single- and few-layer PTI nanosheets.

PTI membrane fabrication

The Anopore membranes (pore size, 20 nm; diameter, 13 mm; Smart Membranes, Halle, Germany) were coated by 15 ml of the coating suspension by vacuum filtration. The coating suspension was prepared by diluting the solution obtained after exfoliation and purification, containing a PTI nanosheet concentration of 0.14 ± 0.06 mg/ml, with more DMAc; sonicating it for 5 min in a bath sonicator (MTI Corporation, Richmond, CA); centrifuging it for 10 min at 10,000*g*; and using the top 13 ml of the supernatant. The volume of concentrated PTI nanosheet solution used for pure PTI membranes was 2 ml and for PTI membranes with *m*-PBI chains as spacers was 1 ml. For PTI membranes with *m*-PBI chains as spacers, the coating solution contained *m*-PBI (0.06 mg/ml). The molecular weight of the *m*-PBI used was 35,000 Da (S10 solution from PBI Performance Products Inc., NC, USA).

Characterizations

Scanning electron microscopy was carried out to observe the surface and cross section of PTI membranes using an FEI Teneo scanning electron microscope with voltages of 1 to 3 kV. All the samples, except for the surface images of the PTI membranes with PBI chains as spacers, were directly characterized without conductive coating. A ~3-nm-thick Ir coating was used for imaging the surface of the PTI membranes with PBI chains as spacers.

The cross section was prepared using focused ion beam (FIB) milling. The sample was coated with a 200-nm protective layer of gold (Q150T Plus, Quorum Technologies) before using XB 540 Crossbeam FIB-SEM (Zeiss) to deposit a 1-μm-thick platinum layer. The sample was tilted to 54°, and a trapezoidal area with 60 and 32 μm for the two bases and a height of 15 μm was milled using 30 kV and 7 nA with a final cutting depth of 10 μm. The trapezoid was milled 3 μm below the deposited platinum. Subsequent cuts were made using a lower current and slowly approaching the deposited platinum. The final cut was carried out using 30 kV and 100 pA.

TEM imaging (bright-field mode) and electron diffraction analysis of the PTI crystals, nanosheets, and membranes were conducted using an FEI Tecnai G2 Spirit Twin microscope with 120 keV incident electron beam energy. Free-standing PTI membrane samples for TEM imaging were prepared by etching the Anopore support in 1 M NaOH, transferring the floating PTI film to a fresh water bath, and picking it up with a 400-mesh copper TEM grid. Thinner PTI films (ca. 200 nm) were used for TEM imaging. HRTEM was performed using either a double Cs-corrected Titan Themis 60-300 microscope (FEI) or a Talos F200X microscope at 80 kV. The filtered images were obtained by applying an adaptive Wiener and a radial difference filters.

AFM measurements were done on a Nanoscope IIIa instrument (Veeco, Santa Barbara, CA, United States) operated in the tapping mode with Nanosensors PPP-NCSTR probes. Data processing was performed using the Gwyddion software. Images were flattened before measuring the height of the nanosheets. The height measurements were well fitted to a log-normal distribution function, and this distribution was used to calculate the mean height of the PTI nanosheets. Samples were prepared by spin-coating a drop of the suspension of PTI nanosheets in DMAc on the surface of a freshly cleaved mica, which was placed afterward in a vacuum oven at 50°C for 3 days.

XPS analysis was performed on a VersaProbe II system (Physical Electronics) using the monochromated Kα x-ray line of an aluminum anode (1486.6 eV). The samples for XPS were prepared by filtering a suspension of PTI nanosheets through an Anopore membrane (pore size, 20 nm) and drying the resulting Anopore membrane with a layer of PTI nanosheets on its surface at 150°C under vacuum for 3 days to remove all the solvents.

XRD measurements were performed in a Bruker D8 Discover x-ray diffractometer equipped with a laser alignment system. Free-standing PTI layers were transferred to a Si low-background sample holder to perform the XRD measurements.

The molecular-sieving performance of PTI membranes was proven using a homemade permeation setup described in detail in a previous publication (*48*). The absolute pressure difference between the feed side and the permeate side of the membrane, for all measurements, was 1 bar to minimize the possible back diffusion of the sweep gas. The pressure on the feed was maintained at 2 bar and on the permeate side at 1 bar during the measurements, unless otherwise specified. All measurements were done after reaching steady state and using argon as the sweep gas. The membranes were sealed with epoxy on a stainless steel annular disk. GC Potting Epoxy from GC Electronics was used for testing up to 150°C, and Scotch-Weld DP760 from 3M was used for testing at higher temperatures. The composition of the permeate was analyzed using a Hiden Analytical HPR-20 mass spectrometer. The membrane cell along with the feed and sweep gas lines were heated inside a convection oven to control the temperature of the measurement. The permeances, *Ji*, of gas *i* were calculated by Eq. 1

$$J_i = X_i/(A \cdot \Delta P_i) \quad (1)$$

where *Xi* is the molar flow rate of component *i* across the membrane area (*A*) and Δ*Pi* is the transmembrane pressure difference for the component *i*. The ideal selectivity *αij* of two gases (*i* and *j*, where *i* is the faster permeating gas) was calculated by Eq. 2

$$\alpha_{ij} = J_i/J_j \quad (2)$$

Ab initio simulations

DFT calculations were performed to optimize the structure of single-layer PTI, calculate the energy barrier of gas molecules passing through the triangular nanopores of single-layer PTI, and describe the electron density isosurfaces of the nanopore. The DFT calculations were performed using the Quantum Espresso package (*49*). Perdew-Burke-Ernzerhof approximation (*50*) was used for the exchange-correlation energy functional. The semiempirical van der Waals correction according to Grimme (*51*) was used. Ultrasoft scalar-relativistic pseudopotentials from the standard solid-state pseudopotentials efficiency library (*52*) were used. The electron wave functions were expanded in plane waves up to an energy cutoff of 60 rydberg (Ry) and a charge density cutoff of 480 Ry. Integration over the Brillouin zone was carried out with a uniform 12 × 12 × 1 *k*-point grids (*53*). A vacuum region of 40 Å was used in the *z* direction to avoid interactions among the periodic replica. The monolayer geometry has been optimized with a threshold of 10^{-4} Ry/au (atomic unit) on the forces and 0.05 kbar on the in-plane pressure, resulting in a theoretical equilibrium lattice parameter of $a = 8.645$ Å. To investigate the potential energy surface (PES) of the chosen gases (i.e., He, H_2, N_2, and CH_4), calculations were performed using 2 × 2 supercells to eliminate spurious interactions between the molecules.

To study the adsorption behavior of gas molecules on the porous PTI monolayer, a constrained relaxation was carried out. The gas molecule was put at different distances from the sheet, and the mass center of the molecule was fixed in the *z* direction (perpendicular to the nanoporous two-dimensional nanosheet). The molecule had the freedom to relax in other directions to find the optimum energy value in each configuration (Fig. 3B), while the PTI geometry was fixed. Typically, for systems like atom-thick PTI hosting only one type of pore, the constrained relaxation method yields similar result as that from computationally expensive methods such as the nudged elastic band (NEB) calculations. For example, fig. S14 compares the PES of H_2 on a PTI nanosheet using constrained relaxation and NEB methods. Overall, the results agree with each other. Moreover, the effects of the approximation used have been checked in a 1 × 1 cell, where it brings substantial changes (i.e., 0.18 eV in the barrier height) only in the PTI-CH_4 case when the hydrogens of CH_4 are at a minimum distance from the PTI hydrogens. For the rest of the molecules and the other CH_4 configuration, it brings negligible changes.

The minimum energy surface for different gas molecules passing through the PTI monolayer was explored using interaction energies between gas molecules and the PTI film. The interaction energies between gas molecules and the PTI monolayer were computed by Eq. 3

$$E_{int} = E_{gas+PTI} - E_{gas(far\ from\ the\ PTI\ membrane)} \quad (3)$$

where $E_{gas\ +\ PTI}$ is the total energy of gas molecules and the PTI monolayer, and $E_{gas(far\ from\ the\ PTI\ membrane)}$ is the energy of molecule and the energy of the PTI monolayer when they do not interact with each other. Because of the strong cohesive force among atoms in the PTI monolayer, it was assumed that the positions of these atoms are fixed during the simulations.

SUPPLEMENTARY MATERIALS

Supplementary material for this article is available at http://advances.sciencemag.org/cgi/content/full/6/4/eaay9851/DC1

Fig. S1. XRD of layered PTI platelets.
Fig. S2. Bright-field TEM image of PTI crystals obtained after one synthesis cycle of 2 days.
Fig. S3. PTI crystal size evolution with synthesis time.
Fig. S4. PTI crystal size evolution with number of synthesis cycles.
Fig. S5. HRTEM of PTI platelets.
Fig. S6. Evolution of the exfoliation of PTI in anhydrous DMAc at 100°C.
Fig. S7. HRTEM images of a single-layer PTI nanosheet.
Fig. S8. HRTEM images of a few-layer PTI nanosheet.
Fig. S9. XPS spectra of PTI nanosheets.
Fig. S10. Interaction of methane molecule with PTI single-layer nanosheet.
Fig. S11. Fabrication of gas-sieving PTI films via vacuum filtration.
Fig. S12. Gas permeation data for PTI membranes.
Fig. S13. Mixed-gas performance of the PTI membranes with *m*-PBI chains as spacers between PTI nanosheets at 250°C.

Fig. S14. PES for H_2 on a PTI monolayer calculated using the NEB and the constrained relaxation methods.
Fig. S15. Diagram showing the selective layer of PTI membranes with *m*-PBI chains as spacers.
Table S1. Elemental analysis of PTI crystals using different synthesis conditions.
Table S2. Li and Cl content on PTI nanosheets.
Table S3. Performance of PTI nanosheet films incorporating *m*-PBI chains at different temperatures.
Supplementary Note I. Carbon nitride membranes fabricated using polymeric melon
Supplementary Note II. Ab initio simulation of interaction between CH_4 and a PTI nanosheet
Supplementary Note III. Calculation of activation energy
Supplementary Note IV. Availability of pores of PTI nanosheets for transport of molecules
Supplementary Note V. Use of *m*-PBI chains as spacers

REFERENCES AND NOTES

1. K. Varoon, X. Zhang, B. Elyassi, D. D. Brewer, M. Gettel, S. Kumar, J. A. Lee, S. Maheshwari, A. Mittal, C.-Y. Sung, M. Cococcioni, L. F. Francis, A. V. McCormick, K. A. Mkhoyan, M. Tsapatsis, Dispersible exfoliated zeolite nanosheets and their application as a selective membrane. *Science* **334**, 72–75 (2011).
2. W.-J. Ong, L.-L. Tan, Y. H. Ng, S.-T. Yong, S.-P. Chai, Graphitic carbon nitride (g-C3N4)-based photocatalysts for artificial photosynthesis and environmental remediation: Are we a step closer to achieving sustainability? *Chem. Rev.* **116**, 7159–7329 (2016).
3. L. Liu, U. Díaz, R. Arenal, G. Agostini, P. Concepción, A. Corma, Generation of subnanometric platinum with high stability during transformation of a 2D zeolite into 3D. *Nat. Mater.* **16**, 132–138 (2017).
4. J. Duan, Y. Li, Y. Pan, N. Behera, W. Jin, Metal-organic framework nanosheets: An emerging family of multifunctional 2D materials. *Coord. Chem. Rev.* **395**, 25–45 (2019).
5. Y. Peng, Y. Li, Y. Ban, H. Jin, W. Jiao, X. Liu, W. Yang, Metal-organic framework nanosheets as building blocks for molecular sieving membranes. *Science* **346**, 1356–1359 (2014).
6. S. Kandambeth, B. P. Biswal, H. D. Chaudhari, K. C. Rout, H. S. Kunjattu, S. Mitra, S. Karak, A. Das, R. Mukherjee, U. K. Kharul, R. Banerjee, Selective molecular sieving in self-standing porous covalent-organic-framework membranes. *Adv. Mater.* **29**, 1603945 (2017).
7. T. Rodenas, I. Luz, G. Prieto, B. Seoane, H. Miro, A. Corma, F. Kapteijn, F. X. Llabrés I Xamena, J. Gascon, Metal–organic framework nanosheets in polymer composite materials for gas separation. *Nat. Mater.* **14**, 48–55 (2015).
8. Y. Peng, Y. Li, Y. Ban, W. Yang, Two-dimensional metal-organic framework nanosheets for membrane-based gas separation. *Angew. Chem. Int. Ed.* **56**, 9757–9761 (2017).
9. H. Zhang, Q. Xiao, X. Guo, N. Li, P. Kumar, N. Rangnekar, M. Y. Jeon, S. Al-Thabaiti, K. Narasimharao, S. N. Basahel, B. Topuz, F. J. Onorato, C. W. Macosko, K. A. Mkhoyan, M. Tsapatsis, Open-pore two-dimensional MFI zeolite nanosheets for the fabrication of hydrocarbon-isomer-selective membranes on porous polymer supports. *Angew. Chem. Int. Ed.* **55**, 7184–7187 (2016).
10. K. Xiao, P. Giusto, L. Wen, L. Jiang, M. Antonietti, Nanofluidic ion transport and energy conversion through ultrathin free-standing polymeric carbon nitride membranes. *Angew. Chem. Int. Ed.* **57**, 10123–10126 (2018).
11. M. Zhao, K. Yuan, Y. Wang, G. Li, J. Guo, L. Gu, W. Hu, H. Zhao, Z. Tang, Metal-organic frameworks as selectivity regulators for hydrogenation reactions. *Nature* **539**, 76–80 (2016).
12. F. Schedin, A. K. Geim, S. V. Morozov, E. W. Hill, P. Blake, M. I. Katsnelson, K. S. Novoselov, Detection of individual gas molecules adsorbed on graphene. *Nat. Mater.* **6**, 652–655 (2007).
13. A. Corma, V. Fornes, S. B. Pergher, T. L. M. Maesen, J. G. Buglass, Delaminated zeolite precursors as selective acidic catalysts. *Nature* **396**, 353–356 (1998).
14. J. Choi, M. Tsapatsis, MCM-22/silica selective flake nanocomposite membranes for hydrogen separations. *J. Am. Chem. Soc.* **132**, 448–449 (2010).
15. T. Moteki, W. Chaikittisilp, Y. Sakamoto, A. Shimojima, T. Okubo, Role of acidic pretreatment of layered silicate RUB-15 in its topotactic conversion into pure silica sodalite. *Chem. Mater.* **23**, 3564–3570 (2011).
16. E. Wirnhier, M. Döblinger, D. Gunzelmann, J. Senker, B. V. Lotsch, W. Schnick, Poly(triazine imide) with intercalation of lithium and chloride ions $[(C_3N_3)_2(NH_xLi1\text{-}_x)_3.LiCl]$: A crystalline 2D carbon nitride network. *Chem. A Eur. J.* **17**, 3213–3221 (2011).
17. M. J. Bojdys, J. O. Müller, M. Antonietti, A. Thomas, Ionothermal synthesis of crystalline, condensed, graphitic carbon nitride. *Chemistry* **14**, 8177–8182 (2008).
18. K. Schwinghammer, B. Tuffy, M. B. Mesch, E. Wirnhier, C. Martineau, F. Taulelle, W. Schnick, J. Senker, B. V. Lotsch, Triazine-based carbon nitrides for visible-light-driven hydrogen evolution. *Angew. Chem. Int. Ed.* **52**, 2435–2439 (2013).
19. T. S. Miller, T. M. Suter, A. M. Telford, L. Picco, O. D. Payton, F. Russell-Pavier, P. L. Cullen, A. Sella, M. S. P. Shaffer, J. Nelson, V. Tileli, P. F. McMillan, C. A. Howard, Single crystal, luminescent carbon nitride nanosheets formed by spontaneous dissolution. *Nano Lett.* **17**, 5891–5896 (2017).
20. D. S. Sholl, R. P. Lively, Seven chemical separations to change the world. *Nature* **532**, 435–437 (2016).
21. R. R. Zolandz, G. K. Fleming, Applications, in *Membrane Handbook*, W. S. W. Ho, K. K. Sirkar, Eds. (Springer US, 1992), pp. 78–94.
22. M. Alders, D. Winterhalder, M. Wessling, Helium recovery using membrane processes. *Sep. Purif. Technol.* **189**, 433–440 (2017).
23. J. Sunarso, S. S. Hashim, Y. S. Lin, S. M. Liu, Membranes for helium recovery: An overview on the context, materials and future directions. *Sep. Purif. Technol.* **176**, 335–383 (2017).
24. L. Zhu, M. T. Swihart, H. Lin, Unprecedented size-sieving ability in polybenzimidazole doped with polyprotic acids for membrane H_2/CO_2 separation. *Energ. Environ. Sci.* **11**, 94–100 (2018).
25. D. R. Pesiri, B. Jorgensen, R. C. Dye, Thermal optimization of polybenzimidazole meniscus membranes for the separation of hydrogen, methane, and carbon dioxide. *J. Membr. Sci.* **218**, 11–18 (2003).
26. K. Ramasubramanian, Y. Zhao, W. S. Winston Ho, CO_2 capture and H_2 purification: Prospects for CO_2-selective membrane processes. *AIChE J.* **59**, 1033–1045 (2013).
27. H. Wang, X. Dong, Y. S. Lin, Highly stable bilayer MFI zeolite membranes for high temperature hydrogen separation. *J. Membr. Sci.* **450**, 425–432 (2014).
28. R. M. de Vos, High-selectivity, high-flux silica membranes for gas separation. *Science* **279**, 1710–1711 (1998).
29. M. Kanezashi, K. Yada, T. Yoshioka, T. Tsuru, Design of silica networks using organic-inorganic hybrid alkoxides for highly permeable hydrogen separation membranes, in *Advances in Bioceramics and Porous Ceramics II*, R. Narayan, P. Colombo, D. Singh, J. Salem, Eds. (John Wiley & Sons Ltd., 2010), pp. 229–239.
30. C. J. Brinker, R. Sehgal, N. K. Raman, S. S. Prakash, L. Delatire, Sol-Gel strategies for controlled porosity ceramic materials: Thin film and bulk. *MRS Proc.* **368**, 329 (1994).
31. H. W. Abu El Hawa, S.-T. B. Lundin, N. S. Patki, J. Douglas Way, Steam methane reforming in a PdAu membrane reactor: Long-term assessment. *Int. J. Hydrogen Energy* **41**, 10193–10201 (2016).
32. S. Yun, J. H. Ko, S. T. Oyama, Ultrathin palladium membranes prepared by a novel electric field assisted activation. *J. Membr. Sci.* **369**, 482–489 (2011).
33. B. A. Mccool, Y. S. Lin, Nanostructured thin palladium-silver membranes: Effects of grain size on gas permeation properties. *J. Mater. Sci.* **36**, 3221–3227 (2001).
34. J. Gascon, F. Kapteijn, B. Zornoza, V. Sebastián, C. Casado, J. Coronas, Practical approach to zeolitic membranes and coatings: State of the art, opportunities, barriers, and future perspectives. *Chem. Mater.* **24**, 2829–2844 (2012).
35. J. Jia, E. R. White, A. J. Clancy, N. Rubio, T. Suter, T. S. Miller, K. McColl, P. F. McMillan, V. Brázdová, F. Corà, C. A. Howard, R. V. Law, C. Mattevi, M. S. P. Shaffer, Fast exfoliation and functionalisation of two-dimensional crystalline carbon nitride by framework charging. *Angew. Chem.* **130**, 12838–12842 (2018).
36. K. Schwinghammer, M. B. Mesch, V. Duppel, C. Ziegler, J. Senker, B. V. Lotsch, Crystalline carbon nitride nanosheets for improved visible-light hydrogen evolution. *J. Am. Chem. Soc.* **136**, 1730–1733 (2014).
37. F. K. Kessler, Y. Zheng, D. Schwarz, C. Merschjann, W. Schnick, X. Wang, M. J. Bojdys, Functional carbon nitride materials—Design strategies for electrochemical devices. *Nat. Rev. Mater.* **2**, 17030 (2017).
38. L. Lin, C. Wang, W. Ren, H. Ou, Y. Zhang, X. Wang, Photocatalytic overall water splitting by conjugated semiconductors with crystalline poly(triazine imide) frameworks. *Chem. Sci.* **8**, 5506–5511 (2017).
39. J. E. Ellis, D. C. Sorescu, S. C. Burkert, D. L. White, A. Star, Uncondensed graphitic carbon nitride on reduced graphene oxide for oxygen sensing via a photoredox mechanism. *ACS Appl. Mater. Interfaces* **9**, 27142–27151 (2017).
40. L. Li, Y. Hu, D. Deng, H. Song, Y. Lv, Highly sensitive cataluminescence gas sensors for 2-butanone based on g-C_3N_4 sheets decorated with CuO nanoparticles. *Anal. Bioanal. Chem.* **408**, 8831–8841 (2016).
41. E. Wirnhier, M. B. Mesch, J. Senker, W. Schnick, Formation and characterization of melam, melam hydrate, and a melam-melem adduct. *Chem. Eur. J.* **19**, 2041–2049 (2013).
42. G. Algara-Siller, N. Severin, S. Y. Chong, T. Björkman, R. G. Palgrave, A. Laybourn, M. Antonietti, Y. Z. Khimyak, A. V. Krasheninnikov, J. P. Rabe, U. Kaiser, A. I. Cooper, A. Thomas, M. J. Bojdys, Triazine-based graphitic carbon nitride: A two-dimensional semiconductor. *Angew. Chem. Int. Ed. Engl.* **53**, 7450–7455 (2014).
43. E. J. McDermott, E. Wirnhier, W. Schnick, K. S. Virdi, C. Scheu, Y. Kauffmann, W. D. Kaplan, E. Z. Kurmaev, A. Moewes, Band gap tuning in poly(triazine imide), a nonmetallic photocatalyst. *J. Phys. Chem. C* **117**, 8806–8812 (2013).
44. J. N. Coleman, M. Lotya, A. O'Neill, S. D. Bergin, P. J. King, U. Khan, K. Young, A. Gaucher, S. De, R. J. Smith, I. V. Shvets, S. K. Arora, G. Stanton, H.-Y. Kim, K. Lee, G. T. Kim, G. S. Duesberg, T. Hallam, J. J. Boland, J. J. Wang, J. F. Donegan, J. C. Grunlan, G. Moriarty, A. Shmeliov, R. J. Nicholls, J. M. Perkins, E. M. Grieveson, K. Theuwissen, D. W. McComb, P. D. Nellist, V. Nicolosi, Two-dimensional nanosheets produced by liquid exfoliation of layered materials. *Science* **331**, 568–571 (2011).
45. C. Zhang, R. Liu, J. Xiang, H. Kang, Z. Liu, Y. Huang, Dissolution mechanism of cellulose in *N,N*-dimethylacetamide/lithium chloride: Revisiting through molecular interactions. *J. Phys. Chem. B* **118**, 9507–9514 (2014).

46. A. Potthast, T. Rosenau, R. Buchner, T. Röder, G. Ebner, H. Bruglachner, H. Sixta, P. Kosma, The cellulose solvent system *N,N*-dimethylacetamide/lithium chloride revisited: The effect of water on physicochemical properties and chemical stability. *Cellulose* **9**, 41–53 (2002).
47. X. Li, R. P. Singh, K. W. Dudeck, K. A. Berchtold, B. C. Benicewicz, Influence of polybenzimidazole main chain structure on H_2/CO_2 separation at elevated temperatures. *J. Membr. Sci.* **461**, 59–68 (2014).
48. G. He, M. Dakhchoune, J. Zhao, S. Huang, K. V. Agrawal, Electrophoretic nuclei assembly for crystallization of high-performance membranes on unmodified supports. *Adv. Funct. Mater.* **28**, 1707427 (2018).
49. P. Giannozzi, S. Baroni, N. Bonini, M. Calandra, R. Car, C. Cavazzoni, D. Ceresoli, G. L. Chiarotti, M. Cococcioni, I. Dabo, A. Dal Corso, S. de Gironcoli, S. Fabris, G. Fratesi, R. Gebauer, U. Gerstmann, C. Gougoussis, A. Kokalj, M. Lazzeri, L. Martin-Samos, N. Marzari, F. Mauri, R. Mazzarello, S. Paolini, A. Pasquarello, L. Paulatto, C. Sbraccia, S. Scandolo, G. Sclauzero, A. P. Seitsonen, A. Smogunov, P. Umari, R. M. Wentzcovitch, QUANTUM ESPRESSO: A modular and open-source software project for quantum simulations of materials. *J. Phys. Condens. Matter* **21**, 395502 (2009).
50. J. P. Perdew, K. Burke, M. Ernzerhof, Generalized gradient approximation made simple. *Phys. Rev. Lett.* **77**, 3865–3868 (1996).
51. S. Grimme, J. Antony, S. Ehrlich, H. Krieg, A consistent and accurate *ab initio* parametrization of density functional dispersion correction (DFT-D) for the 94 elements H-Pu. *J. Chem. Phys.* **132**, 154104 (2010).
52. G. Prandini, A. Marrazzo, I. E. Castelli, N. Mounet, N. Marzari, Precision and efficiency in solid-state pseudopotential calculations. *npj Comput. Mater.* **4**, 72 (2018).
53. H. J. Monkhorst, J. D. Pack, Special points for Brillouin-zone integrations. *Phys. Rev. B* **13**, 5188–5192 (1976).

Acknowledgments: We thank P. Bugnon for performing the sealing of the quartz ampules under high vacuum and T. LaGrange for assistance during HRTEM imaging and image filtering. We are grateful to S. Huang for participation in valuable discussions and for sharing expertise in the transfer and handling of thin freestanding films. **Funding:** We thank our host institution, EPFL, for support. Parts of the work were funded by the Swiss National Science Foundation (Assistant Professor Energy Grant; grant number PYAPP2_173645) and the Swiss Competence Center for Energy Research: Efficiency of Industrial Processes (SCCER-EIP). We thank the Swiss National Supercomputing Center, CSCS, for the allocation of computing resources (production project s860). D.C. and N.M. acknowledge support from the MARVEL NCCR. D.C. acknowledges support from the EPFL Fellows program co-funded by M. Sklodowska-Curie, Horizon 2020 grant agreement number 66566. **Author contributions:** K.V.A. and L.F.V. conceived the project. L.F.V. designed, prepared, and characterized PTI crystals, nanosheets, and PTI-based membranes. M.T.V. performed the DFT calculations with help and guidance from D.C. and N.M. FIB characterization and mixed-gas pressure stability tests were performed by M.D. Z.N. prepared large batches of PTI crystals. M.M. performed XPS and AFM experiments. L.F.V. and E.O. characterized PTI with HRTEM, and E.O. generated the simulated HRTEM image of single-layer PTI using JEMS. L.F.V. and K.V.A. wrote the manuscript. All authors revised the paper. **Competing interests:** K.V.A. and L.F.V. have filed a patent application based on these findings. The authors declare no other competing interests. **Data and materials availability:** All data needed to evaluate the conclusions in the paper are present in paper and/or the Supplementary Materials. Additional data related to this paper may be requested from the authors.

Submitted 3 August 2019
Accepted 21 November 2019
Published 24 January 2020
10.1126/sciadv.aay9851

Citation: L. F. Villalobos, M. T. Vahdat, M. Dakhchoune, Z. Nadizadeh, M. Mensi, E. Oveisi, D. Campi, N. Marzari, K. V. Agrawal, Large-scale synthesis of crystalline g-C_3N_4 nanosheets and high-temperature H_2 sieving from assembled films. *Sci. Adv.* **6**, eaay9851 (2020).

Science Advances

Large-scale synthesis of crystalline g-C_3N_4 nanosheets and high-temperature H_2 sieving from assembled films

Luis Francisco Villalobos, Mohammad Tohidi Vahdat, Mostapha Dakhchoune, Zahra Nadizadeh, Mounir Mensi, Emad Oveisi, Davide Campi, Nicola Marzari and Kumar Varoon Agrawal

Sci Adv **6** (4), eaay9851.
DOI: 10.1126/sciadv.aay9851